

Geometrically navigating topological plate modes around gentle and sharp bends

Mehul P. Makwana^{1,2}, Richard V. Craster¹

¹ *Department of Mathematics, Imperial College London, London SW7 2AZ, UK and*

² *Multiwave Technologies AG, 3 Chemin du Prê Fleuri, 1228, Geneva, Switzerland*

Predictive theory to geometrically engineer devices and materials in continuum systems to have desired topological-like effects is developed here by bridging the gap between quantum and continuum mechanical descriptions. A structured elastic plate, a bosonic-like system in the language of quantum mechanics, is shown to exhibit topological valley modes despite the system having no direct physical connection to quantum effects. We emphasise a predictive, first-principle, approach, the strength of which is demonstrated by the ability to design well-defined broadband edge states, resistant to backscatter, using geometric differences; the mechanism underlying energy transfer around gentle and sharp corners is described. Using perturbation methods and group theory, several distinct cases of symmetry-induced Dirac cones which when gapped yield non-trivial band-gaps are identified and classified. The propagative behavior of the edge states around gentle or sharp bends depends strongly upon the symmetry class of the bulk media and we illustrate this via numerical simulations.

I. INTRODUCTION

There has been considerable recent activity in wave phenomena motivated through topological effects: The critical realisation has been that fundamental ideas originating in topological insulators and quantum mechanics [1–3], based around the Schrödinger equation, carry across, in some regards, to continuous wave systems based around, say, the Maxwell equations, such as topological photonic and phononic crystals [4, 5]. Much of the recent continuum literature draws very heavily upon that from quantum mechanics and it is important to note that some care is required in this translation.

Similar care is required in dealing with the delicacies and repercussions of group theoretic concepts [6–9]. We will go back to first principles and elucidate key details in the translation process, and in group theory, highlighting and clarifying common issues that arise within structured elastic plates and by extension to other periodic crystal structures such as those in photonics or phononics. A recurrent theme throughout the article is the power of group theory in terms of clarifying and classifying, *a priori* without any explicit calculation, when certain effects will occur in classical waves.

The fields of group theory and topology transcend specific physical systems, hence the phenomena we describe translate widely. However, there are naturally technical differences and we choose to illustrate our theory within the context of flexural waves upon thin structured elastic plates [10], by doing so we emphasise the continuum nature of the model and show the generality of the basic ideas: It has no connection with quantum mechanics in either its formulation or theoretical basis. Thin plate flexural wave theories, as described in [11, 12] are highly effective physical models for elastic waves in plates and have proved to be reliable in predictions of many wave phenomena for structured plates [13], plate models utilising Dirac cones in the style of graphene [14], illustrating cloaking [15], negative refraction [16] and valley edge states [17]. Typically flexural wave theory, for homogeneous plates, is quoted as only being accurate for wavelengths greater than 20 times the plate thickness [18] which is rather limiting. However, as shown in [13], it is the wavelength in the periodic system that

actually matters, and that can be large compared to the plate thickness, even at high frequencies. These plate models also act in practical terms as motivation for seismic metamaterial applications [19, 20]. Gaining understanding of the interaction of sub-wavelength arrays of resonators with an underlying plate [21, 22] enabled these concepts to carry across to full vector elastic systems involving Rayleigh waves [23]. Similarly, plate models are also critical in terms of highlighting features such as zero-frequency stopbands [24] that can then be used to try and design broadband seismic phononic shields that can function at the long-wave and low-frequency regimes that are of importance in that context [25–27].

The elastic plate model is ideal in terms of describing and modelling topological effects as many results for point scatterers are available explicitly [28]. A particularly pleasant feature of analysis using this model is that the fundamental Green's function is, unlike in acoustics, electromagnetism and vector elasticity, non-singular and it remains bounded. This means we can concentrate cleanly upon issues such as group theory, and its influence upon the effects we see, without numerical distractions. The plate model, unlike acoustic and electromagnetic counterparts, has wave dispersion even when homogeneous and thus exemplifies the ubiquitous nature of the effects we discuss.

There are two canonical types of topological insulators, those which preserve time reversal symmetry (TRS) and those which break it. In quantum mechanics the design of a TRS insulator is contingent upon the fractional spin of the fermions. Quantitatively, this condition requires that the time-reversal operator squares to -1 ; this is different to Newtonian systems that consist of spin-1 bosonic-like particles. In the absence of spin-half particles for our system, we leverage the pseudospins inherent in hexagonal lattices that have broken inversion symmetry. The binary valley degree of freedom can be used to design valleytronic devices similar to those in spintronics by leveraging the valley-pseudospin in the manner of electron spin. The prohibition of backscattering is reliant upon there being no intervalley scattering hence the valley Hall effect [29–32] of our system here is unlike the quantum Hall effect that breaks TRS; as our valley Hall insulators do not

break TRS they are far more straightforward to realise.

In the topological context, care must be taken when navigating waves around bends as we must prohibit hybridisation of modes with opposite pseudo-spin. Transport of energy around corners in structured media is of inherent interest [33–35]. We simultaneously require that the incoming edge mode can couple into a mode, that must exist, along the interface after the corner. Critically the existence of that mode is dependent upon the geometrical properties of the elementary cells of the structured media and their relative arrangement. Within these constraints we now proceed to construct valley-dependent edge states that enable the suppression of intervalley scattering along the zigzag boundary, leading to valley-protected broadband robust transport around a bend.

We begin in Sec. II by explicitly recasting the continuum plate model into the language of quantum mechanics, utilising a Hamiltonian description, whilst retaining elements of the continuum language to bridge across the quantum and elastic plate communities. In Sec. III we demonstrate the geometrical differences in propagation around gentle and sharp bends which adjoin topologically distinct media. Concluding remarks are drawn together in section IV.

II. ELASTIC PLATE CRYSTALS

We consider the elastic plate analogues of photonic, or phononic, crystals where a homogeneous plate is given structure by a lattice of defects which could be holes, pillars, mass-spring resonators or elastic rods; familiar effects such as forbidden frequency band-gaps and dynamic anisotropy all emerge within this plate system. We choose to use the simplest defects, that is we either use clamped points, “pins”, of zero radius or mass-loading at a point and both are common idealisations for point scatterers [28]. Resonators attached at the lattice vertices [14, 17, 36] could easily be added into the formalism we present, but introduce an unnecessary additional physical feature associated with resonance; using point-scatterers, that are either simple masses or constrained, demonstrate that resonance is not required in order to obtain topological effects.

A. Formulation

The flexural wave modes that exist on an infinite elastic plate with constraints at lattice points are characterised by their vertical displacement, $\psi_{n\kappa}(\mathbf{x})$. The subscript notation denotes that this field variable is dependent upon the Bloch-wavevector κ and n is an index that numbers the eigenmodes.

These displacement eigenmodes are governed by the (non-dimensionalised) Kirchhoff-Love (K-L) equation

$$[H_{KL} - \mu(\mathbf{x})\omega_{\kappa}^2] \psi_{n\kappa} = F(\mathbf{x}), \quad (1)$$

where we introduce the operator H_{KL} as

$$H_{KL} = \nabla_{\mathbf{x}}^2 [\beta(\mathbf{x}) \nabla_{\mathbf{x}}^2] \quad (2)$$

and the reaction forces at the point constraints $F(\mathbf{x})$ introduce the dependence upon the direct lattice. The quantities $\mu(\mathbf{x})$ and $\beta(\mathbf{x})$ represent variations in the non-dimensional mass per unit length and flexural rigidity of the plate respectively; their spatial dependence respects the same periodicity as the lattice of point constraints.

The simplest constraints are those of point mass-loading with the reaction forces proportional to the displacement via an impedance coefficient and thus

$$F(\mathbf{x}) = \omega_{\kappa}^2 \sum_{\mathbf{n}} \sum_{p=1}^P M_{\mathbf{n}}^{(p)} \psi_{n\kappa}(\mathbf{x}) \delta(\mathbf{x} - \mathbf{x}_{\mathbf{n}}^{(p)}). \quad (3)$$

Here \mathbf{n} labels each elementary cell, containing $p = 1 \dots P$ constraints, that periodically repeats to create the infinite physical plate crystal. The mass in cell \mathbf{n} at point constraint p is given by $M_{\mathbf{n}}^{(p)}$. This constraint automatically encompasses the point pinned plate crystal, as the limit $\omega_{\kappa}^2 M_{\mathbf{n}}^{(j)} \rightarrow \infty$, where the reaction forces are retained

$$F(\mathbf{x}) = \sum_{\mathbf{n}} \sum_{p=1}^P F_{\mathbf{n}}^{(p)} \delta(\mathbf{x} - \mathbf{x}_{\mathbf{n}}^{(j)}) \quad (4)$$

but the displacement is constrained explicitly to be zero at the pins, i.e. $\psi_{n\kappa}(\mathbf{x}_{\mathbf{n}}^{(p)}) = 0$.

More generally, it is convenient to use the eigenstate notation for the K-L equation as

$$\hat{H} |\psi_{n\kappa}\rangle = \hat{\mu}(\mathbf{x})\omega_{\kappa}^2 |\psi_{n\kappa}\rangle + F(\mathbf{x}) |\psi_{n\kappa}\rangle, \quad (5)$$

where the component equation (1) is retrieved from Eq. (5) using

$$\hat{H} = \int |\mathbf{x}\rangle H(\mathbf{x}, \mathbf{y}) \langle \mathbf{y}| d\mathbf{x}d\mathbf{y}, \quad H(\mathbf{x}, \mathbf{y}) = \delta(\mathbf{x} - \mathbf{y})H_{KL}.$$

In an infinite medium the displacements are Bloch eigenfunctions

$$\psi_{n\kappa}(\mathbf{x}) = \langle \mathbf{x} | \psi_{n\kappa} \rangle = \exp(i\kappa \cdot \mathbf{x}) \langle \mathbf{x} | u_{n\kappa} \rangle,$$

where $|u_{n\kappa}\rangle$ is a periodic eigenstate. The displacements satisfy the following completeness and orthogonality relations:

$$\sum_{n\kappa} |\psi_{n\kappa}\rangle \langle \psi_{n\kappa}| = \hat{1}, \quad \langle \psi_{n\kappa} | \psi_{m\kappa'} \rangle = \delta_{mn} \delta_{\kappa, \kappa'}. \quad (6)$$

Due to the periodic arrangement of the inclusions, the displacement response, in Eq. (1), naturally encourages a Fourier representation

$$\psi_{n\kappa}(\mathbf{x}) = \sum_{\mathbf{G}} W(\mathbf{G}) \exp(i(\mathbf{G} - \kappa) \cdot \mathbf{x}). \quad (7)$$

as a sum over reciprocal lattice vectors \mathbf{G} . This gives the formal solution in reciprocal space via

$$(|\mathbf{G} - \kappa|^4 - \omega_{\kappa}^2) W(\mathbf{G}) = \frac{\omega_{\kappa}}{A_{PC}} \sum_{p=1}^P M_{\mathbf{I}}^{(p)} \psi_{n\kappa}(\mathbf{x}_{\mathbf{I}}^{(p)}) \exp[-i(\mathbf{G} - \kappa) \cdot \mathbf{x}_{\mathbf{I}}^{(p)}], \quad (8)$$

where \mathbf{I} denotes an arbitrary reference cell in physical space, A_{PC} is the area of the primitive cell and, for clarity, we do not allow for spatial dependence of physical parameters. This formulation is convenient for numerical simulation, and we use an adaptation [36] of the plane wave expansion method [37] to determine the eigenstates.

B. Perturbation theory

We now apply the $\mathbf{k} \cdot \mathbf{p}$ perturbation method [38, 39] to the system (1) whereby we retrieve the perturbed eigensolutions as a function of those at a reference point in Fourier space. Initially, we define a new complete orthogonal set, namely, the Kohn-Luttinger functions as,

$$\chi_{n\kappa}(\mathbf{x}) = \exp(i\kappa \cdot \mathbf{x}) \chi_{n\kappa_0}(\mathbf{x}), \quad (9)$$

where κ_0 is a fixed wavevector. Similar to $\psi_{n\kappa}(\mathbf{x})$, they form a complete orthogonal basis set, (6). Using the Kohn-Luttinger functions, we can expand any Bloch state, $\psi_{n\kappa}(\mathbf{x})$, in the complete orthogonal basis set $\{\chi_{j\kappa}(\mathbf{x})\}$,

$$|\psi_{n\kappa}\rangle = \sum_j A_{nj}(\kappa) |\chi_{j\kappa}\rangle = \exp(i\Delta\kappa \cdot \mathbf{x}) \sum_j A_{nj}(\kappa) |\psi_{j\kappa_0}\rangle \quad (10)$$

and $\Delta\kappa = \kappa - \kappa_0$. After inserting the expansion into the governing equation we obtain the integrand,

$$\exp(i\Delta\kappa \cdot \mathbf{x}) \sum_j A_{nj}(\kappa) [(\omega_{\kappa_0}^2 - \omega_{\kappa}^2) \times \left[\mu(\mathbf{x}) + \sum_{\mathbf{N}, p} M_{\mathbf{N}}^{(p)} \delta(\mathbf{x} - \mathbf{x}_{\mathbf{N}}^{(p)}) \right] + \Delta\kappa \cdot \hat{\mathbf{p}}_{\mathbf{x}} + \mathcal{O}(|\Delta\kappa|^2)] \psi_{j\kappa_0}(\mathbf{x}) = 0. \quad (11)$$

The momentum operator is explicitly given by

$$\hat{\mathbf{p}}_{\mathbf{x}} = 2i [\nabla_{\mathbf{x}}^2 \beta(\mathbf{x}) \nabla_{\mathbf{x}} + 3\nabla_{\mathbf{x}} \beta(\mathbf{x}) \nabla_{\mathbf{x}}^2 + 2\beta(\mathbf{x}) \nabla_{\mathbf{x}}^3] \quad (12)$$

and the orthogonality of the eigensolutions, (6), is written as,

$$\langle \psi_{n\kappa} | \psi_{m\kappa'} \rangle = \frac{(2\pi)^2}{A_{PC}} \int_{PC} \psi_{n\kappa}^*(\mathbf{x}) \mu(\mathbf{x}) \psi_{m\kappa'}(\mathbf{x}) d\mathbf{x} = \delta_{mn} \delta_{\kappa, \kappa'}, \quad (13)$$

where the integral is taken over the primitive cell. Motivated by the orthogonality relation we multiply (11) by $\psi_{l\kappa_0}^*(\mathbf{x})$ and integrate over the primitive cell to get

$$\sum_j (H_{lj} - (\omega_{\kappa}^2 - \omega_{\kappa_0}^2) \Lambda_{lj}) A_{nj}(\kappa) = 0, \\ H_{lj} = \Delta\kappa \cdot \mathbf{p}_{lj} + \mathcal{O}(|\Delta\kappa|^2), \quad \mathbf{p}_{lj} = \langle \psi_{l\kappa_0} | \hat{\mathbf{p}}_{\mathbf{x}} | \psi_{j\kappa_0} \rangle, \\ \Lambda_{lj} = \delta_{lj} + \sum_p M_{\mathbf{I}}^{(p)} \psi_{l\kappa_0}^*(\mathbf{x}_{\mathbf{I}}^{(p)}) \psi_{j\kappa_0}(\mathbf{x}_{\mathbf{I}}^{(p)}) \quad (14)$$

Nontrivial eigensolutions exist if the following secular equation is satisfied,

$$\det [H - (\omega_{\kappa}^2 - \omega_{\kappa_0}^2) \Lambda] = 0. \quad (15)$$

To retrieve the full dispersion relation, the entire basis set at κ_0 , would need to be considered. However, if we are solely interested in linear dispersions around Dirac- and Dirac-like cones then the summation is limited to the degenerate Bloch states (as these eigensolutions, collectively, form an orthogonal degenerate subspace). Hence after neglecting second- and higher-order terms, (14) is simplified to,

$$\sum_{j=1}^d [H_{lj}^{(1)} - 2\omega_{\kappa_0} \Delta\omega \Lambda_{lj}] A_{nj}(\kappa) = 0, \\ \Delta\omega = \omega_{\kappa} - \omega_{\kappa_0} = \Delta\kappa \cdot \nabla_{\kappa} \omega_{\kappa_0} + \mathcal{O}(|\Delta\kappa|^2), \\ H_{lj}^{(1)} = \Delta\kappa \cdot \mathbf{p}_{lj}, \quad (16)$$

where d is the degree of degeneracy. From this we see that the first-order term is exclusively determined by the strength of the coupling between the degenerate Bloch states. Other non-degenerate states contribute to higher-order corrections [6]. No assumption has been made on the origins of the degeneracy; therefore the above equation is applicable to both, essential and accidental, degeneracies with linear dispersive behaviour. As an alternative to the Kohn-Luttinger model we could have opted to expand $|\psi_{n\kappa_0}\rangle$ into its constituent plane-waves [40] to obtain the same result.

C. Symmetry induced Dirac cones

In this subsection we rectify and extend basic group theoretical concepts, found in [41], that aid us in the reduction of the Hamiltonian. All the space group elements, which leave our lattice invariant, are succinctly written as $\{R, \tau\}$; where R denotes a point group symmetry element and τ corresponds to a lattice translation. The triangular-like periodic structures, under consideration here, belong to a symmorphic space group G ; hence all $\{R, \tau\} \in G$ are compound symmetries obtained by combining a point group element and a primitive lattice translation. Specifically, the elements in G are separable, $\{R, \tau\} = \{R, 0\} \{\varepsilon, \tau\}$; where τ denotes a Bravais lattice translation. It follows that the plane wavefunctions satisfy the following equalities,

$$\hat{P}_{\{R, \tau\}} \psi_{n\kappa}(\mathbf{x}) = \hat{P}_{\{R, 0\}} \hat{P}_{\{\varepsilon, \tau\}} \psi_{n\kappa}(\mathbf{x}) = \exp(i\hat{R}\kappa \cdot \tau) \psi_{n\hat{R}\kappa}(\mathbf{x}), \quad (17)$$

where \hat{R} denotes the operator form of R . If we are at a high-symmetry point in the Brillouin zone then $\hat{R}\kappa = \kappa \bmod \mathbf{G}$, for many different \hat{R} , where \mathbf{G} is an arbitrary reciprocal lattice vector. Each \hat{R} , which satisfies this transformation property at κ , belongs to the group of the wavevector, denoted by G_{κ} . The wavevector group of highest symmetry is G_{Γ} which is

isomorphic to the factor group G/T ; T is the translation subgroup. Hence, any non-zero wavevector group is a (normal) subgroup of G_Γ ; notationally this is written as $G_\kappa \triangleleft G_\Gamma$. At high-symmetry points in Fourier-space, deterministic degeneracies form, which yield a degenerate set of eigenfunctions $\{\psi_{n\hat{R}\kappa}(\mathbf{x})\}$, which correspond to the same frequency. In the following two subsections we shall use the point group symmetries, at the KK' valleys, to simplify the Hamiltonian found in Eq. (16).

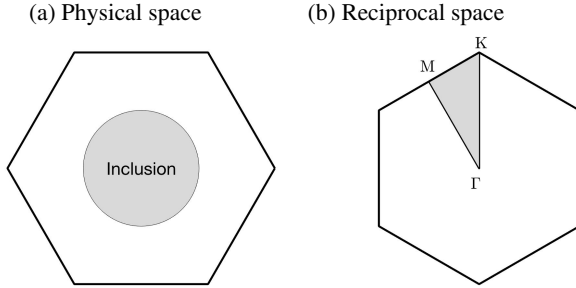


Figure 1: Wigner-Seitz cell in physical and reciprocal space. Shaded region, in the latter, indicates the IBZ.

Symmetries for the Brillouin zone of an unperturbed system are given by the group $C_{6v} = C_6 + 3\sigma_v (+3\sigma_d)$, where the two distinct families of mirror symmetries, namely the vertical (σ_v) and dihedral (σ_d), are shown in Fig. 2. The corners of the Brillouin zone are associated with the point groups $C_{3v} = C_3 + 3\sigma_v$, C_3 ; where the dependency on $3\sigma_d$ (if present) is dropped as the symmetry does not contribute to gapping the Dirac cone. For the point group C_{3v} (see table II) we ascertain, immediately, that the KK' valleys always support Dirac cones. The symmetries at Γ are also immediately found, as $C_{3v} \triangleleft G_\Gamma$, therefore $G_\Gamma = C_{6v}$ or C_{3v} . Examples, of hexagonal lattices that have these symmetries are shown, as the first two rows, in table I. For continuous systems, containing a periodic array of scatterers, it is sufficient to solely consider a hexagonal cell with a single inclusion; the benefits of the honeycomb or Kagome structures are in the additional degrees of freedom that they offer when analysing discrete analogues of continuous systems [42–46]. Hence, for simplicity, we primarily consider the single ‘inclusion’ case from hereon. Additionally, to have explicit solutions we use point scatterers in place of finite radii inclusions; where the point scatterers are placed at the vertices of the ‘inclusion’. It is also sufficient to consider the illustrative examples, of triangular and hexagonal inclusions, as all permutations that yield Dirac cones (and which gap them) are distilled down into these two distinct shapes.

Unlike the point group C_{3v} , the C_3 point group supports a deterministic Dirac cone if and only if $G_\Gamma = C_6$. In this instance, the two complex one-dimensional representations in table III stick together due to the presence of TRS. Let us demonstrate this fact by considering the point group of an arbitrary element κ_0 . If an element $g \in G_\Gamma$ such that $g : \kappa_0 \rightarrow -\kappa_0$ then clearly $g^2 \in G_{\kappa_0}$. Now, if the inversion operator $\hat{\pi} \in G_{\kappa_0}$ then $\{g\} \in G_{\kappa_0}$ and, trivially, we are at Γ

where we obtain a non-degenerate quadratic curve. However if $\hat{\pi} \notin G_{\kappa_0}$ then g may or may not belong to G_{κ_0} , hence a test is required to discern which of the above cases is satisfied. The test conducted is known as Herring’s criterion [7] and is succinctly written as,

$$\sum_{\{g\}} \chi(g^2) = \begin{cases} h_g, & \text{no additional degeneracy,} \\ 0, -h_g & \text{doubling of degeneracy,} \end{cases} \quad (18)$$

where $\chi(g^2)$ is a character associated to a specific irreducible representation (IR) in G_{κ_0} and h_g is the number of elements in $\{g\}$. This test is used to determine whether or not TRS introduces any additional degeneracies. Returning to our specific case, let $\kappa_0 = K$ or K' ; now since $\hat{\pi} \notin C_3$ we proceed with Herring’s criterion. If $G_\Gamma = C_6$ then $\{g\} = \{C_2, C_6, C_6^{-1}\}$. In other words, these are the only elements within C_6 which transform K to its TR counterpart K' and vice-versa. Squaring these elements we find that $\{C_2^2, C_6^2, C_6^{-2}\} = \{E, C_3, C_3^{-1}\}$; next we perform Herring’s criterion by using table III,

$$\chi(E) + \chi(C_3) + \chi(C_3^{-1}) = 1 + \epsilon + \epsilon^2 = 0, \quad (19)$$

where $\epsilon = \exp(2\pi i/3)$; this is the second case in (18) therefore if $G_\Gamma = C_6$ we get a double degeneracy due to the presence of TRS. Similarly, this test can be carried out for $G_\Gamma = C_{3v}$, where $\{g\} = \{3\sigma_v\}$, $\sum \chi(g^2) = h_g$ which is the first case hence when $\{G_\Gamma, G_{KK'}\} = \{C_{3v}, C_3\}$ we obtain a non-degenerate quadratic curve.

In summary, the three sets of symmetries that yield deterministic Dirac cones are $\{G_\Gamma, G_{KK'}\} = \{C_{6v}, C_{3v}\}$, $\{C_{3v}, C_{3v}\}$, $\{C_6, C_3\}$. Examples of structures yielding these symmetry sets are shown in table I.

Table I: Hexagonal Lattice Dirac Cones

Case	G_Γ	$G_{K,K'}$	Example Inclusions	$K \leftrightarrow K'$
(i)	C_{6v}	C_{3v}	Hexagonal, $\lambda = \epsilon^n$	$\{\sigma_v\}, \hat{\pi}$
(ii)	C_{3v}	C_{3v}	Triangular, $\lambda = \epsilon^{2n}$	$\{\sigma_v\}$
(iii)	C_6	C_3	Hexagonal, $\lambda \neq \epsilon^n$	$\hat{\pi}$

The three cases: Here λ is the angle of rotation away from the vertical axis and $\epsilon = \exp(i\pi/6)$. The column $K \leftrightarrow K'$ indicates whether the mirror $\{\sigma_v\}$ and/or inversion $\hat{\pi}$ symmetries map K to K' (and vice versa).

D. Hamiltonian reduction

By using the group theoretic principles espoused in the previous section we can further reduce the Hamiltonian of Eq. (16). Due to the invariance of a scalar product to symmetry operations, applying \hat{R} to an arbitrary wavevector, κ , is equivalent to applying its inverse operator \hat{R}^{-1} to the physical space vector, \mathbf{x} . Therefore for an $R \in G_{\kappa_0}$, Eq. (17) can

be written as,

$$\begin{aligned}\hat{P}_R \psi_{j\kappa_0}(\mathbf{x}) &= \psi_{j\hat{R}\kappa_0}(\mathbf{x}) = \psi_{j\kappa_0}(\hat{R}^{-1}\mathbf{x}) \\ &= \sum_{i=1}^d D(R)_{i,j} \psi_{i\kappa_0}(\mathbf{x}),\end{aligned}\quad (20)$$

where $D(R)$ is an irreducible matrix representation (IMR) which relates the basis functions in an IR

$$\hat{P}_R |\psi_{j\kappa}\rangle = \sum_{i=1}^d D(R)_{i,j} |\psi_{i\kappa}\rangle. \quad (21)$$

Motivated by Eq. (20), we apply a change of variables, namely $\mathbf{y} = \hat{R}^{-1}\mathbf{x}$, to \mathbf{p}_{lj} in (14),

$$\begin{aligned}\mathbf{p}_{lj} &= \int_{\text{PC}} \psi_{i\kappa_0}^*(\mathbf{y}) \hat{\mathbf{p}}_{\mathbf{y}} \psi_{j\kappa_0}(\mathbf{y}) d\mathbf{y} \\ &= \hat{R}^{-1} \sum_{m,n} D^*(R)_{l,m} D(R)_{n,j} \mathbf{p}_{mn},\end{aligned}\quad (22)$$

as well as to Λ_{lj} ,

$$\Lambda_{lj} = \sum_{m,n} D^*(R)_{l,m} D(R)_{n,j} \Lambda_{mn}. \quad (23)$$

Recall that, as we are dealing with orthogonal transformations, the Laplacian is invariant under a change of basis; hence (22) is true for any system with an even-ordered governing equation. Eq. (22) relates different matrix elements within the first-order correction, hence the perturbed Hamiltonian is reduced using the point group symmetries at κ_0 .

Directly from the form of \mathbf{p}_{lj} , in (14), we immediately ascertain that the matrix \mathbf{p} is Hermitian. Therefore, for the doubly degenerate case, of the Dirac cone we get $\mathbf{p}_{12} = \mathbf{p}_{21}^*$. Restricting ourselves to symmetry induced Dirac cones we need only to consider the point groups $C_3 = \{e, C_3, C_3^2\}$ and $C_{3v} = C_3 + 3\sigma_v$. The point group C_3 supports two independent complex one-dimensional IR's; see table III. As mentioned earlier, by Herring's criterion; the pair of one-dimensional complex IRs join to yield a double-degeneracy if (and only if) the point group at Γ is C_6 ; the resulting two-dimensional IMRs of the rotation operators are identical, up to a similarity transformation, to those found in C_{3v} (see App. B). As $G_{KK'} = C_3$ or C_{3v} and $C_3 \triangleleft C_{3v}$, we opt to initially reduce the Hamiltonian by using the rotation operators belonging to C_3 ; additionally, due to the equivalence of the representations E , for both C_3 and C_{3v} , we use the same IMR, see Eq. (B1) in App. B.

After substituting $\hat{R} = \pm \hat{C}_3$ into (22), we arrive at the following relations,

$$\begin{aligned}\mathbf{p}_{11} &= -\mathbf{p}_{22}, & \mathbf{p}_{12} &= \mathbf{p}_{21}, & \mathbf{p}_{12} &= -i\hat{\sigma}_y \mathbf{p}_{11}, \\ \Lambda_{11} &= \Lambda_{22}, & \Lambda_{12} &= \Lambda_{21} = 0,\end{aligned}\quad (24)$$

where $\hat{\sigma}_y$ is the second Pauli matrix; the final equation in (24) indicates that \mathbf{p}_{11} and \mathbf{p}_{12} are orthogonal. The Pauli matrices

along with the identity matrix form a basis for the vector space of 2×2 Hermitian matrices; they are defined as,

$$\hat{\sigma}_a = \begin{bmatrix} \delta_{a,z} & \delta_{a,x} - i\delta_{a,y} \\ \delta_{a,x} + i\delta_{a,y} & -\delta_{a,z} \end{bmatrix}, \quad (25)$$

where $a = x, y, z$. Using the relations (24) we simplify the Hamiltonian, found in Eq. (16), to the following,

$$H^{(1)} = -|\Delta\kappa||\mathbf{p}_{11}| \begin{bmatrix} -\cos\theta & \sin\theta \\ \sin\theta & \cos\theta \end{bmatrix}, \quad (26)$$

where θ is the angle between $\Delta\kappa$ and \mathbf{p}_{11} . Somewhat unexpectedly (24) and (26) are identical to those for photonic crystals in [41]. Herein we have demonstrated that they hold for all even-ordered two-dimensional systems. Using the reduced Hamiltonian and (16) we find the gradient near the KK' valleys, in addition to, the first-order frequency correction,

$$2\omega_{\kappa_0} \Delta\omega \Lambda_{11} = \pm |\Delta\kappa||\mathbf{p}_{11}| \implies \frac{\Delta\omega}{|\Delta\kappa|} = \pm \frac{|\mathbf{p}_{11}|}{2\omega_{\kappa_0}} \Lambda_{11}. \quad (27)$$

Note Eq. (27) is angular-independent; therefore the linear slopes, near Dirac cones, are independent of the reflectional properties of the system. However, if we are dealing with a system which has C_{3v} symmetry, at the KK' points, then the set of three equivalent reflections $3\sigma_v$ are used to simplify the Hamiltonian (26) further by specifying the angular component.

The IMR associated to the element $\sigma_v \in C_{3v}$ is proportional to the third Pauli matrix $\hat{\sigma}_z$ (see App. B for more details). Therefore, if $G_{KK'} = C_{3v}$ we substitute $\hat{R} = \hat{\sigma}_z$ into Eq. (22) which yields,

$$H_{\text{unpert}}^{(1)} = \tau_z v_D (\hat{\sigma}_z \Delta\kappa_x - \hat{\sigma}_x \Delta\kappa_y), \quad (28)$$

where the group velocity is,

$$v_D = \frac{|\mathbf{p}_{11}|}{2\omega_{\kappa_0}} \Lambda_{11}, \quad (29)$$

$\tau_z = \pm 1$ is the valley spin index, which corresponds to the KK' valleys, respectively. The connection between the τ_z term and the KK' valleys is seen explicitly by substituting in the binary rotation about the z -axis C_2 into (22); this transforms K into K' . The plate Hamiltonian (28) resembles that of a massless Dirac fermion; it acts upon the amplitudes of the Kohn-Luttinger functions (9) which, themselves, have been expanded around a degenerate pair of eigenstates (10). Note that, alternatively, the Hamiltonian could have been reduced using selection rules [6, 47].

Due to the simplified form of the reduced Hamiltonian, (26), the Berry phase is immediately retrievable [48, 49]. This phase factor, defined as,

$$\begin{aligned}\phi &= i \oint \langle \psi_{n\kappa} | \nabla_{\mathbf{x}} | \psi_{n\kappa} \rangle \cdot d\mathbf{l} = \\ &= i \oint \sum_j A_{nj}^*(\kappa) \nabla_{\kappa} A_{nj}(\kappa) \cdot d\mathbf{l},\end{aligned}\quad (30)$$

impacts wave transport properties when there is interaction between different Bloch eigenstates. The Kohn-Luttinger functions, in (30), are analytically derivable by substituting the perturbed Hamiltonian (26) into the eigenvalue problem (16). In turn, these are substituted into the Berry phase formula (30) thereby yielding the expected result, for Dirac cones, $\phi = \pi$. The relevance of this result was shown in [47] where for Dirac-like cones $\phi = 0$ whilst for pure Dirac cones, $\phi = \pm\pi$. In a perfectly periodic medium, both, Dirac and Dirac-like cones are associated to perfect transmission of an incident wave through the medium; this is due to the locally linear curves which yield dispersionless waves. The physical ramifications of the difference in Berry phase present themselves in the presence of a defect whereby a zero Berry phase is associated with normal localisation whilst a system with a Berry phase of $\pm\pi$ implies antilocalisation effects. Under PT-symmetry, the Berry phase is quantized such that $\phi = \pi n$ hence no perturbation can continuously change it. In order to destroy a Dirac point, you either, move two Dirac points together which have opposite flux or you break parity and/or TRS. In the next section we shall break parity symmetry to gap the Dirac point, thereby yielding non-trivial band gaps.

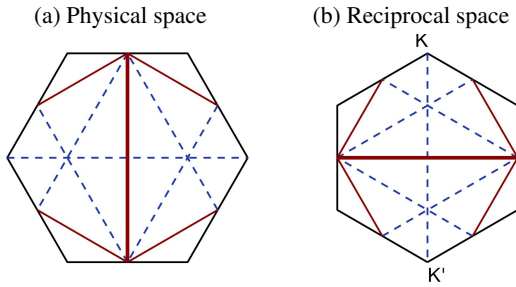


Figure 2: The two sets of reflectional symmetries: $\{\sigma_d\}$ and $\{\sigma_v\}$ (solid lines) in the physical and reciprocal spaces respectively. Similarly $\{\sigma_v\}$, $\{\sigma_d\}$ are shown dashed in physical and reciprocal space [50].

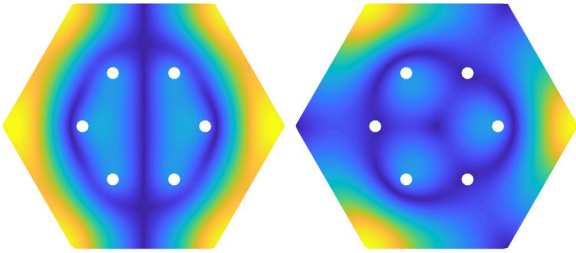


Figure 3: Symmetry breaking at K : the left and right panels show the absolute value of the displacement at the ungapped, and gapped Dirac point of case (i), shown in Fig. 5, for $\omega = 16.5$.

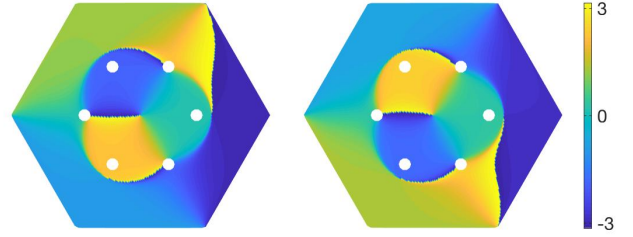


Figure 4: The chirality of the separated valley states at K (left panel) and K' (right panel) for the gapped Dirac point of case (i) shown in Fig. 5, $\omega = 16.5$ showing the intrinsic circular-polarized orbital angular momentum using the phase distribution of the field.

E. Perturbed Hamiltonian and the valley Chern number

We now demonstrate, from first-principles, how the Hamiltonian is altered when a Dirac point is gapped. We then immediately retrieve (local) topological quantities in the vicinity of the KK' valleys that indicate the existence of topological valley modes.

For simplicity, we consider the honeycomb structure, comprised of the AB sublattices, that, when unperturbed, has the system symmetries $\{C_{6v}, C_{3v}\}$. The other two Dirac point gapping perturbations, used in the subsequent section, arise from changing mass values and/or positions; their perturbed Hamiltonian is obtained in a very similar manner. Returning to the honeycomb structure, the effective Hamiltonian is given in (28) and the associated eigenvalues are shown in (27). When perturbed, the mass term in (3) is expanded as,

$$\begin{aligned} M_{A,B} &= M_{av} + dM(x_{A,B}) = M_{av} \pm \alpha\Delta M, \\ M_{av} &= \frac{M_A + M_B}{2}, \quad \Delta M = \frac{|M_A - M_B|}{2}, \end{aligned} \quad (31)$$

where, hereafter, we assume that ΔM is of the same order as $|\Delta\kappa|$. The leading-order M_{av} part is independent of the AB sublattices and retains the C_{6v} symmetry of the unperturbed crystal. After substituting (31) into (11) the bracketed mass term is altered to,

$$\sum_{\mathbf{N},p} \delta(\mathbf{x} - \mathbf{x}_{\mathbf{N}}^{(p)}) [(\omega_{\kappa_0}^2 - \omega_{\kappa}^2)M_{av} + \omega_{\kappa_0}^2 dM(x_{A,B})]. \quad (32)$$

Consequently $M^{(p)}$ is replaced with, the p independent term, M_{av} up until (28). The additional perturbative term, within the bracket, in (16) is,

$$d\Lambda_{lj} = \sum_{p=A,B} \omega_{\kappa_0}^2 dM(x_p) \psi_{i\kappa_0}^*(\mathbf{x}_p) \psi_{j\kappa_0}(\mathbf{x}_p). \quad (33)$$

If $M_A \neq M_B$ then the point group symmetry at the KK' valleys is reduced to C_3 hence the Dirac point is gapped. This

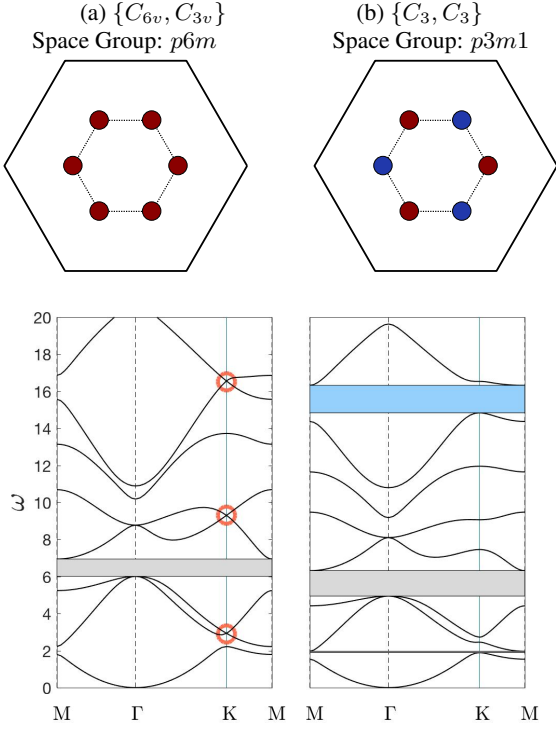


Figure 5: Case (i) in table I generated by perturbing masses, showing the geometry, space groups and dispersion curves of (a) unperturbed and (b) perturbed cases: Unperturbed (perturbed) mass value 1 (2) the norm of basis vectors is 2 and distance from center of cell to masses is 0.5 In (a) the Dirac points are circled and in (b) the new bandgap created by gapping the Dirac point is shaded blue.

is due to the breakdown in parity symmetry between the valleys in Fourier space and is reflected in the symmetry reduced counterpart to (23),

$$d\Lambda_{lj} = - \sum_{m,n} D^*(\sigma_v)_{l,m} D(\sigma_v)_{n,j} d\Lambda_{mn}. \quad (34)$$

Using this, and (28), the perturbed effective Hamiltonian takes the form,

$$H_{\text{eff}}^{(1)} = H_{\text{unpert}}^{(1)} + \tau_z M_K \hat{\sigma}_y, \quad M_K = \omega_{\kappa_0}^2 \Delta M, \quad (35)$$

hence, due to the presence of τ_z , $M_K = -M_{K'}$. The corresponding eigenvalues for this effective Hamiltonian are,

$$(\omega_{\kappa_0}^2 - \omega_{\kappa}^2) = \pm \sqrt{v_D^2 |\Delta \kappa|^2 + M_K^2}. \quad (36)$$

This is precisely the form of the eigenvalues for the massive Dirac fermionic equation albeit, here, it is for a plate crystal. The, now, non-zero Dirac mass term in (36) implies locally quadratic curvature. Following similar arguments to [40] we evaluate the Chern number as $C = C_K + C_{K'}$ where $C_{K,K'} = \text{sgn}(M_{K,K'})/2 = \pm \phi/2$; the first relation arises because the greatest modal contribution emanates from the KK' valleys; the latter relation, with ϕ , becomes evident after applying Stokes theorem to the Berry phase (30). Due to

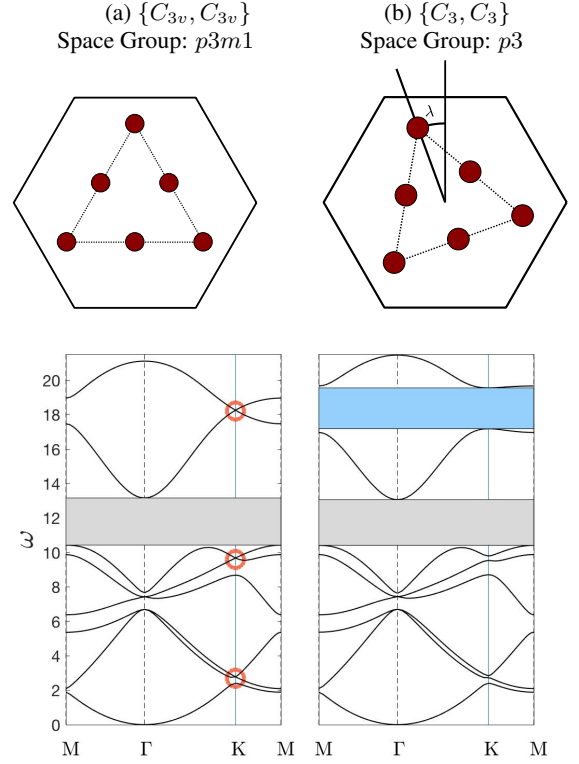


Figure 6: Case (ii) of table I, generated by an angular perturbation of $\lambda = 0.05$, showing the geometry, space groups and dispersion curves of (a) unperturbed and (b) perturbed cases: the norm of basis vectors is 2 and distance between cell center and vertices of triangle is 0.8. In (a) the Dirac points are circled and in (b) the new bandgap created by gapping the Dirac point is shaded blue.

the presence of the valley matrix index, τ_z , in (36) it follows that the Chern number vanishes; therefore a globally nontrivial topology is not permitted within the framework of our effective theory. However, the non-zero topological quantities at each of the valleys indicates that edge states, with limited backscattering, are possible as long as the hybridisation of the two valley modes is controlled.

III. ENGINEERING TOPOLOGICAL VALLEY STATES IN PLATE CRYSTALS

A. Symmetry reduction

The three sets of symmetries, table I, give rise to deterministic Dirac cones. The systematic reduction in symmetry of a plate crystal will gap the Dirac points thereby yielding a band gap. More specifically, for cases (i) and (ii), by reducing $G_{KK'}$ from C_{3v} down to the symmetry set C_3 (or lower) we are assured of a pair of non-degenerate quadratic curves at the KK' valleys. For case (i), if $G_{KK'} = C_3$ then we would have to ensure that G_Γ did not have six-fold symmetry. Case (iii) already has $G_{KK'} = C_3$ and the task is to lower the G_Γ

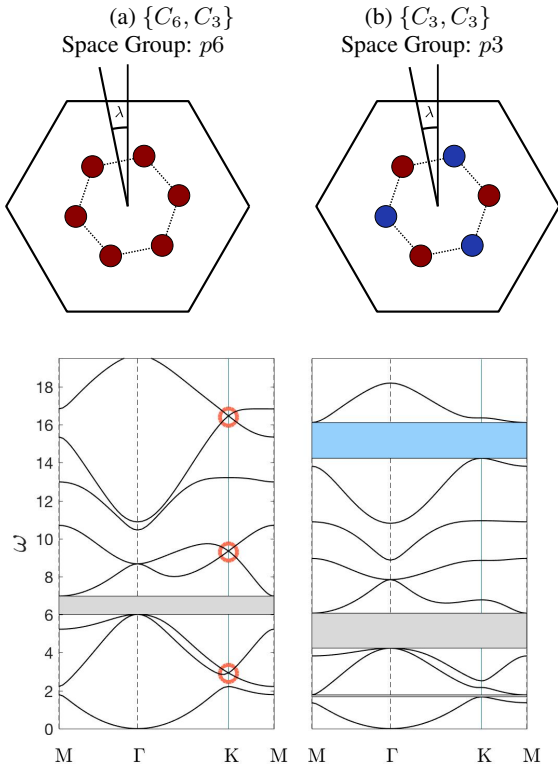


Figure 7: Case (iii) in table I, generated by perturbing masses and geometry, showing the geometry, space groups and dispersion curves of (a) unperturbed and (b) perturbed cases: Angular deviation λ , from cell symmetry axis, is 0.15; unperturbed mass value is 1, perturbed mass value is 2. Norm of basis vectors is 2 and distance between cell center and masses is 0.5. In (a) the Dirac points are circled and in (b) the new bandgap created by gapping the Dirac point is shaded blue.

symmetry set by breaking inversion symmetry.

Consider cases (i) and (ii) of table I which, for an unperturbed system, have $\{C_{6v}, C_{3v}\}$ or $\{C_{3v}, C_{3v}\}$ symmetries; these two are reduced down to the symmetry set $\{C_{3v}, C_3\}$ or lower. The appropriate symmetry breaking, for these cases, occurs when the mirror symmetry set $\{\sigma_v\}$ (and, for case (i), inversion symmetry as well) is removed in reciprocal space. Removing these mirror symmetries $\{\sigma_v\}$ c.f. Fig. 2 is equivalent to the removal of $\{\sigma_d\}$ in physical space (see Fig. 3). This is evident in the eigensolutions, shown in Fig. 3, which demonstrate the symmetry breaking in physical space. The gapped Dirac points result in eigensolutions which have opposite chirality at the KK' valleys, Fig. 4; this opposite pseudospin between the valleys is represented by τ_z in Eq. (35). A canonical example of this symmetry breaking occurs for the honeycomb structure when the alternating sublattice mass values are made inequivalent; similar to Fig. 5. Conversely, removing $\{\sigma_d\}$ symmetries in Fourier space preserves the Dirac point, as $G_{KK'} = C_{3v}$, and hence there are no gapped states. For example, if the cellular structure of Fig. 5(b) is rotated by $\pi/6$ the Dirac point will remain ungapped, despite inversion

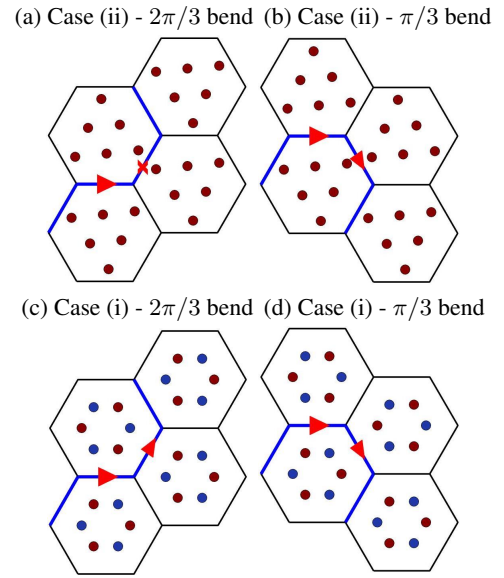


Figure 8: The detail of the junction cells, showing their asymmetric edges, for the cases we consider.

symmetry being broken, as the $\{\sigma_v\}$ symmetries remain.

Simple examples for the systematic reductions of all three symmetry sets, and analysis of the resulting topological states, are given in the subsequent sections. In particular Fig. 5(a) shows case (i), $\{C_{6v}, C_{3v}\}$, reduced to $\{C_3, C_3\}$ by the simple act of breaking reflectional symmetry through alternating the masses; case (ii) $\{C_{3v}, C_{3v}\}$ has symmetry broken by rotating the inner triangular arrangement. Case (iii), with the unperturbed state as $\{C_6, C_3\}$, is slightly different to the other two cases as $G_{KK'}$ is already C_3 and only supports a deterministic Dirac cone if $G_\Gamma = C_6$; hence the reduction of G_Γ to C_3 is sufficient to gap the Dirac cone. Fig. 7 shows the consequence of breaking the C_6 symmetry at Γ , in this case alternating the masses removes inversion symmetry.

Figs 5, 6, 7 show the bandstructures for the cases of interest. The positions in reciprocal space we choose deserve a note of detail regarding time-reversal invariant systems. From the cell configurations shown in Figs 5, 6, 7 only the configuration in Fig. 5(a) reduces down to the IBZ, shown in Fig. 1, with just the use of its spatial symmetries. The presence of TRS permits a further folding, on top of the spatial symmetries, thereby yielding an IBZ having the $p6m$ space group IBZ.

Several papers have discussed how different inclusion shapes affect the bandgap width [51–53]. Although no systematic rules can be drawn from these numerical studies several factors appear to significantly impact the presence and width of bandgaps. [54] showed that the largest absolute photonic bandgap is achieved by selecting an inclusion of the same symmetry as the cell. Other factors influencing the gap width are the orientation and size of the inclusions.

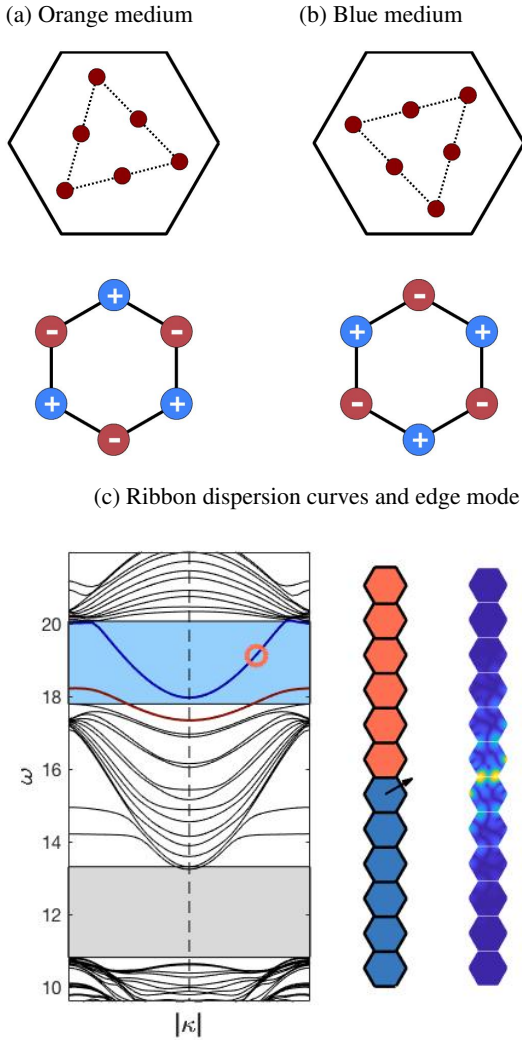


Figure 9: Plate zero-line mode. (a) and (b) showing the upper and lower media (case (ii) of Table I as shown in Fig. 6(b) for the upper medium and its rotation by $\pi/3$ for the lower medium), see Fig. 8(a), and the sign of the valley Chern numbers at the KK' points. (c) shows the dispersion curves with the edge mode lying in the bandgap, $\omega = \{17.79, 20.07\}$, and at the highlighted frequency $\omega = 19.13$, we show the edge mode in physical space.

B. Plate zero-line modes

The perturbation of the media has broken the six-fold symmetry whilst retaining three-fold symmetry. This results in asymmetric behaviour at the edges (and vertices) of the perturbed cellular structures. Due to the broken parity symmetry we now have inequivalent KK' valleys, and moreover the valley Chern numbers are opposite in sign (τ_z in Eq. (35)). Creating interfaces between two media that have opposite Chern numbers, at a particular valley, will generate valley Hall edge states, [31]; these are aptly named zero-line modes (ZLMs) due to the opposite Chern numbers either side of the inter-

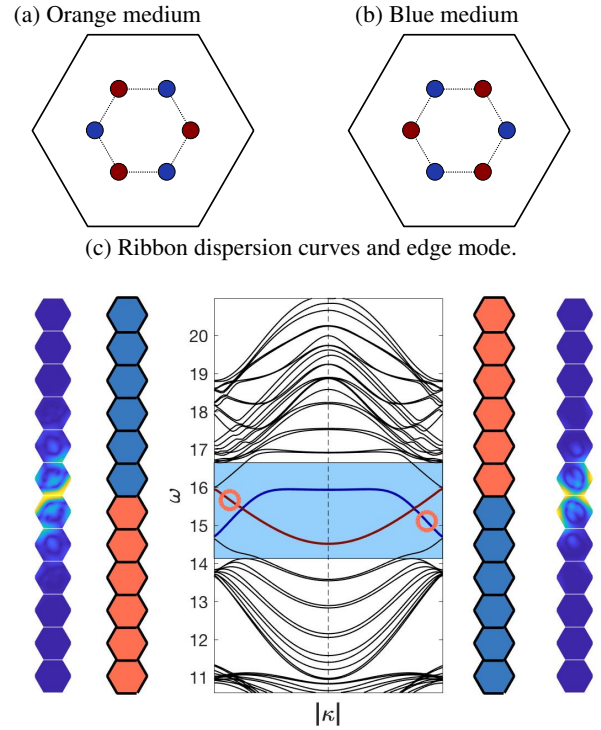


Figure 10: Plate zero-line mode. (a) and (b) showing the upper and lower media (case (i) of Table I as shown in Fig. 5(b) for the upper medium and its rotation by $\pi/3$ for the lower medium), see Fig. 8(b). (c) shows the dispersion curves with the edge modes lying in the bandgap, $\omega = \{14.13, 16.65\}$, and at the highlighted frequencies $\omega = 15.11, 15.67$, we show the edge modes in physical space.

face. A convenient approach for creating such media is to take advantage of the lack of six-fold symmetry and join one perturbed medium to its $\pi/3$ rotated twin. A benefit of these valley Hall modes is that we have *a priori* knowledge of how to construct the two adjoining media (sharing a bandgap) such that we are guaranteed broadband edge modes.

To compute the ZLMs we adapt the plane wave expansion method, (8), by extending it to a finite, long, ribbon of hexagons (as shown in the inset to Fig. 9). We need only consider Bloch conditions in the direction indicated by the arrow shown in the hexagonal ribbon of Fig. 9. Numerically, we consider a long ribbon and extract solutions that decay exponentially; we apply periodic conditions at the top/bottom of the ribbon and convergence is checked by mode doubling and extending the ribbon.

The three-fold symmetry of the perturbed structures, resulting in asymmetric edges, yields two distinct interfaces between two topologically distinct media; these distinct edges are shown in Fig. 8. ZLMs are shown for two different geometrical cases; namely, cases (i) and (ii). For the latter, we obtain the edge modes shown in Fig. 9; the broadband mode pertains to the orange cell over the blue cell, whilst the narrow band mode, below it, comes from flipping the cells i.e. the

blue over orange; the different interfaces between the media coincide with the two distinct edges. The limited overlap between the two modes implies that for a large frequency range these modes do not couple into each other. This property will be used for filtering waves in section III C.

In contrast, Fig. 10 for case (i) has two overlapping broadband modes. Unlike case (ii) both the edge modes for orange over blue (and vice versa) exist over a simultaneous frequency range. The distinction in the edges is reflected in the different modal patterns shown in Fig. 10. The differences, between cases (i) and (ii), emerge from the degree of asymmetry of the cell's edges. The large distance between the centroid and the vertices of the triangular inclusion for case (ii) results in an almost effective barrier to wave transport (see Fig. 8 (a) and (b)); this is unlike case (i) (Fig. 8 (c) and (d)).

C. Transport around sharp edges

To illustrate the consequences of particular cellular structures, we now examine the propagative behaviour around gentle and sharp bends of angles $2\pi/3, \pi/3$ respectively. Our simulations use the explicit Green's function to create a linear system that is rapidly evaluated as in [14, 28].

Initially, we analyse the gentle bend, Fig. 11(a), and we launch a ZLM at the leftmost interface towards the bend. No-

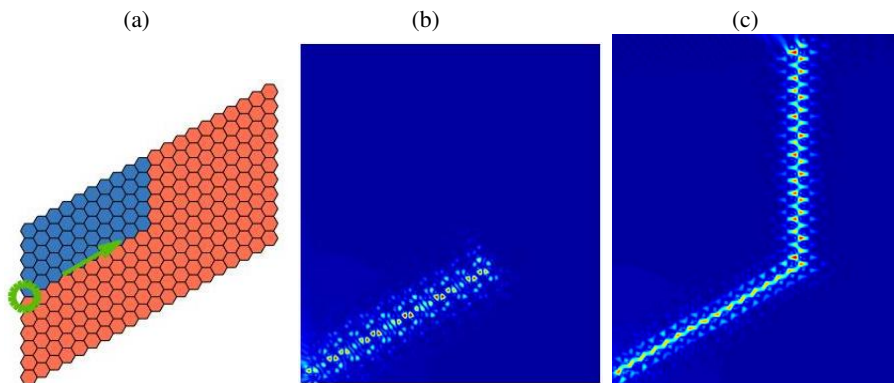


Figure 11: ZLM transport around a gentle bend ($2\pi/3$ angle), schematic in (a). Panels (b) and (c) show the absolute value of displacements for case (ii) C_{3v} , and case (i) C_{6v} respectively. The detail of the ZLM pre- and post-bend in (c) is of note. 1890 cells were used, excitation frequency for C_{3v} case was $\omega = 19.53$, and C_{6v} case $\omega = 15.19$.

IV. CONCLUDING REMARKS

We have shown, using group and $\mathbf{k}\cdot\mathbf{p}$ theory, a first-principles approach to creating plate topological valley modes for all two-dimensional hexagonal lattices. For the elastic plate crystal, this allows for there to be a direct bridge between the quantum and continuum mechanical worlds. Group theory allowed us to identify three distinct geometrical cases having symmetry induced Dirac cones; the correct breaking of parity symmetry revealed nontrivial band-gaps in which broadband edge modes reside. Given such edge modes it is natural to consider the transport of energy around bends in partitioned media. It becomes clear when doing so that the details of the

junction cells, in the vicinity of the bend, are significant. One important issue that we have not considered here is that of disorder, [55] consider this and it would be interesting to explore this carefully for the ZLMs presented here. The asymmetry of the edges at cells, between the topologically distinct media, indicates two different mechanisms of energy transport around bends; the success of the strategy we employ is seen through the clarity of states demonstrated numerically.

Armed with this knowledge of how to design really clean and sharp edge states, and the underlying principles at the junction cells, this will motivate the design of more efficient interfacial waveguides, topological networks and energy filters, using the different cases we have identified: Experimen-

Turning our attention to the sharp bend, Fig. 12; from Fig. 8(b) and (d), along with the discussion in the previous paragraph, one would naively expect similar behaviour to that of the gentle bend. However this is not the case as the zigzag edges pre- and post-bend are identical; this is more easily seen from the scattering Figs. 12 rather than the cellular arrangement, Fig. 8 (b) and (d). Additionally a new phenomena, tunnelling, plays a role. These properties are numerically indicated in Fig. 12, in particular note how the clarity of the modes allows us to see with ease that the modal patterns pre- and post-bend, are identical, for both geometrical cases.

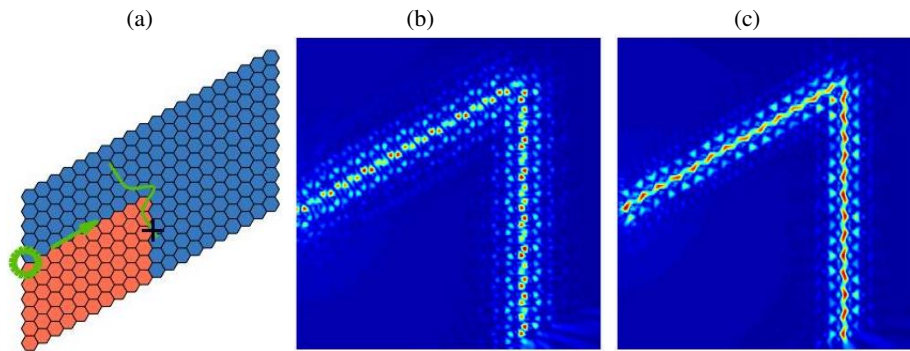


Figure 12: ZLM transport around a sharp bend ($\pi/3$ angle), schematic in (a). Panels (b) and (c) show the absolute value of displacements for case (ii) C_{3v} , and case (i) C_{6v} respectively. The details of the ZLM pre- and post-bends are of note. 1890 cells were used, excitation frequency for C_{3v} case was $\omega = 19.18$, and C_{6v} case $\omega = 15.09$.

tal verification of these results is encouraged.

a Leverhulme Trust Research Fellowship.

ACKNOWLEDGEMENTS

The authors thank the EPSRC for their support through grant EP/L024926/1 and R.V.C acknowledges the support of

-
- [1] C. L. Kane and E. J. Mele, *Phys. Rev. Lett.* **95**, 146802 (2005).
[2] M. Z. Hasan and C. L. Kane, *Rev. Mod. Phys.* **82**, 3045 (2010).
[3] Y. Ren, Z. Qiao, and Q. Niu, *Rep. Prog. Phys.* **79**, 066501 (2016).
[4] L. Lu, J. D. Joannopoulos, and M. Soljacic, *Nature Photonics* **8**, 821 (2014).
[5] A. B. Khanikaev and G. Shvets, *Nat. Photonics* **11**, 763 (2017).
[6] M. S. Dresselhaus, G. Dresselhaus, and A. Jorio, *Group theory: application to the physics of condensed matter* (Springer-Verlag, 2008).
[7] T. Inui, Y. Tanabe, and Y. Onodera, *Group Theory and Its Applications in Physics* (Springer-Verlag, 1990).
[8] H. Dai, T. Liu, J. Jiao, B. Xia, and D. Yu, *Journal of Applied Physics* (2017).
[9] J. Lu, S. X. Chunyin Qiu, Y. Ye, M. Ke, and Z. Liu, *Phys. Rev. B* (2014).
[10] R. C. McPhedran, A. B. Movchan, and N. V. Movchan, *Mech. Mat.* **41**, 356 (2009).
[11] L. D. Landau and E. M. Lifshitz, *Theory of elasticity*, 2nd ed. (Pergamon Press, 1970).
[12] K. F. Graff, *Wave motion in elastic solids* (Oxford University Press, 1975).
[13] G. Lefebvre, T. Antonakakis, Y. Achaoui, R. Craster, S. Guenneau, and P. Sebbah, *Phys. Rev. Lett.* **118**, 254302 (2017).
[14] D. Torrent, D. Mayou, and J. Sanchez-Dehesa, *Phys. Rev. B* **87**, 115143 (2013).
[15] M. Farhat, S. Guenneau, and S. Enoch, *Phys. Rev. Lett.* **103**, 024301 (2009).
[16] M. Farhat, S. Guenneau, S. Enoch, A. Movchan, and G. Petrusson, *Appl. Phys. Lett.* **96**, 081909 (2010).
[17] R. K. Pal and M. Ruzzene, *New J. Phys.* **19**, 025001 (2017).
[18] L. R. F. Rose and C. H. Wang, *J. Acoust. Soc. Am.* **116**, 154 (2004).
[19] S. Brule, E. Javelaud, S. Enoch, and S. Guenneau, *Phys. Rev. Lett.* **112** (2014).
[20] A. Colombi, P. Roux, S. Guenneau, P. Gueguen, and R. V. Craster, *Sci. Reps.* **6**, 19238 (2016).
[21] A. Colombi, P. Roux, and M. Rupin, *J. Acoust. Soc. Am.* **136**, EL192 (2014).
[22] E. G. Williams, P. Roux, M. Rupin, and W. A. Kuperman, *Phys. Rev. B* **91**, 104307 (2015).
[23] A. Colombi, D. Colquitt, P. Roux, S. Guenneau, and R. V. Craster, *Sci. Rep.* **6**, 27717 (2016).
[24] A. B. Movchan, N. V. Movchan, and R. C. McPhedran, *Proc. R. Soc. Lond. A* **463**, 2505 (2007).
[25] S. Krodel, N. Thome, and C. Daraio, *Ext. Mech. Lett.* **4**, 111 (2015).
[26] M. Miniaci, A. Krushynska, F. Bosia, and N. M. Pugno, *New J. Phys.* **18**, 083041 (2016).
[27] Y. Achaoui, T. Antonakakis, S. Brûlé, R. V. Craster, S. Enoch, and S. Guenneau, *New J. Phys.* **19**, 063022 (2017).
[28] D. V. Evans and R. Porter, *J. Engng. Math.* **58**, 317 (2007).
[29] J.-W. Dong, X.-D. Chen, H. Zhu, Y. Wang, and X. Zhang, *Nature Materials* **16**, 298 (2017).
[30] H. Zhu, T.-W. Liu, and F. Semperlotti, *Phys. Rev. B* **97** (2018), arXiv: 1712.10271.
[31] D. Xiao, W. Yao, and Q. Niu, *Phys. Rev. Lett.* **99**, 236809 (2007).
[32] X.-D. Chen, F.-L. Zhao, M. Chen, and J.-W. Dong, *Phys. Rev. B* **96**, 020202(R) (2017).
[33] A. Mekis, J. C. Chen, I. Kurland, S. Fan, P. R. Villeneuve, and J. D. Joannopoulos, *Phys. Rev. Lett.* **77**, 3787 (1996).
[34] T. Ma, A. B. Khanikaev, S. H. Mousavi, and G. Shvets, *Phys. Rev. Lett.* **114** (2015).
[35] A. Chutinan, M. Okano, and S. Noda, *Appl. Phys. Lett.* **80**, 1698 (2002).

- [36] Y. Xiao, J. Wen, and X. Wen, J. Phys. D: Appl. Phys. **45**, 195401 (2012).
- [37] S. G. Johnson and J. D. Joannopoulos, Optics Express **8**, 173 (2001).
- [38] C. T. C. Jun Mei, Ying Wu and Z.-Q. Zhang, Phys. Rev. B (2012).
- [39] J. L. Janssen, Y. Gillet, S. Ponc, A. Martin, M. Torrent, and X. Gonze, Phys. Rev. B **93** (2016), arXiv: 1708.05890.
- [40] T. Ochiai, Phys. Rev. B **86** (2012).
- [41] J. Lu, C. Qiu, S. Xu, Y. Ye, M. Ke, and Z. Liu, Phys. Rev. B **89** (2014).
- [42] L. Zhang and Q. Niu, Phys. Rev. Lett. (2017).
- [43] Y. Liu, Y. Xu, S.-C. Zhang, and W. Duan, Phys. Rev. B **96**, 064106 (2017).
- [44] Y. Liu, Y. Xu, and W. Duan, National Science Review **5**, 314 (2018).
- [45] H. Guo and M. Franz, Phys. Rev. B **80**, 113102 (2009).
- [46] X. Ni, M. A. Gorlach, A. Alu, and A. B. Khanikaev, New J. Phys **19**, 055002 (2017).
- [47] J. Mei, Y. Wu, C. T. Chan, and Z.-Q. Zhang, Phys. Rev. B **86**, 035141 (2012).
- [48] M. Berry, Proc. R. Soc. Lond. A **392**, 45 (1984).
- [49] D. Xiao, M.-C. Chang, and Q. Niu, Rev. Mod. Phys. **82**, 1959 (2010).
- [50] G. Vasseur, Y. Fagot-Revurat, B. Kierren, M. Sicot, and D. Malterre, Symmetry **5**, 344 (2013).
- [51] R. Min, F. Wu, L. Zhong, H. Zhong, S. Zhong, and Y. Liu, J. Phys. D: Appl. Phys. **39**, 2272 (2006).
- [52] Y.-Z. Wang, F.-M. Li, W.-H. Huang, and Y.-S. Wang, J. Phys: Cond. Mat. **19**, 496204 (2007).
- [53] Y.-F. Wang, Y.-S. Wang, and X.-X. Su, J. Appl. Phys. **110**, 113520 (2011).
- [54] R. Wang, X.-H. Wang, B.-Y. Gu, and G.-Z. Yang, J. Appl. Phys. 4307 (2001).
- [55] Y. Jin, D. Torrent, B. and Djafari-Rouhani, Phys. Rev. B 054307 (2018).

V. APPENDICES

Appendix A: Character tables

Classes → IR ↓	E	$2C_3$	$3\sigma_v$	Basis Functions	
				Odd-Parity	Even-Parity
E	2	-1	0	$\{x, y\}$ $\{h_1(x, y), h_2(x, y)\}$	$\{x^2 - y^2, 2xy\}$ $\{(x^2 - y^2)^2 - 4x^2y^2, xy(x^2 - y^2)\}$

Table II: Selected row and basis functions of C_{3v} character table.

Classes → IR ↓	E	C_3	C_3^2	Basis Functions	
				Odd-Parity	Even-Parity
E	1	ϵ	ϵ^2	$\{x, y\}$ $\{h_1(x, y), h_2(x, y)\}$	$\{x^2 - y^2, 2xy\}$ $\{(x^2 - y^2)^2 - 4x^2y^2, xy(x^2 - y^2)\}$

Table III: Selected row and basis functions of C_3 character table; $\epsilon = \exp(2\pi i/3)$.

Appendix B: Irreducible representation matrices

IMR for three-fold rotations:

$$D_E(\pm C_3) = \begin{bmatrix} -1/2 & \mp\sqrt{3}/2 \\ \pm\sqrt{3}/2 & -1/2 \end{bmatrix}. \quad (\text{B1})$$

This IMR is for the odd-parity basis $\{x, y\}$ which is chosen because it simplifies equation (22) moreso than its even-parity counterpart $\{x^2 - y^2, 2xy\}$; due to the property $\pm\hat{C}_3 = D_E(\pm C_3)$. As we are seeking to examine the local behaviour in the vicinity of the Dirac cone, either parity basis may be used, as they are both associated to the same IR.

The IMR of σ_v , shown in table II, is explicitly,

$$D_E(\sigma_v) = -\hat{\sigma}_z, \quad (\text{B2})$$

where $\hat{\sigma}_z$ is the third Pauli matrix; this representation implies that σ_v is the parity transformation $\kappa_y \rightarrow -\kappa_y$.

We have shown that for KK' valleys with C_3 symmetry we get a deterministic Dirac cone if and only if $G_\Gamma = C_6$. In

this instance, the sticking together of the two one-dimensional complex representations yields IMR's of the form,

$$D'_E(R) = \begin{bmatrix} \omega & 0 \\ 0 & \omega^2 \end{bmatrix}, \quad (\text{B3})$$

which is equivalent to the C_{3v} rotation matrices after undergoing an equivalence transformation,

$$D_E(R) = UD'_E(R)U^{-1}, \quad U = \frac{1}{\sqrt{2}} \begin{bmatrix} i & -i \\ 1 & 1 \end{bmatrix}, \quad (\text{B4})$$

therefore the form of the perturbed Hamiltonian, after reduction using rotational symmetries, is identical for systems which have C_3 and C_{3v} point group symmetry at KK' .